Feedback optimization strategy for rotational alignment echo spectroscopy

Manon Bournazel, Antoine Espaignol, Pierre Béjot, Edouard Hertz, Franck Billard, Olivier Faucher

Abstract The recent discovery of rotational echoes has contributed to extend the applications of field-free molecular alignment to short time scales, namely to a temporal region preceding the first alignment revival of the molecule. Most echo measurements require adjusting the position of the echo over time, which in case of molecular alignment echo unavoidably leads to a change in its amplitude, unless the intensity of the pulse sequence triggering the echo is properly modified. Here, we propose to avoid this drawback by using an optical pulse shaper steered by a learning algorithm. We demonstrate that a temporal shaping, whose characteristics are optimized to maintain a constant echo amplitude regardless of its creation time, can be generated by controlling the spectral phase and amplitude of the laser pulse which are then used in an open-loop control system. As a proof of principle, the optimization strategy is applied to the observation of short term dissipative dynamics of laser aligned molecules exposed to collisions and to the measurement of associated decoherence and population decay time constants.

Feedback optimization strategy for rotational alignment echo spectroscopy

Manon Bournazel[1], Antoine Espaignol[1], Pierre Béjot[1], Edouard Hertz[1], Franck Billard[1], and O. Faucher[1,*]

1. Introduction

Since their discovery [1], rotational alignment echoes have stimulated significant interest in the ultrafast science community [2–18]. The attention paid to this new phenomenon is mainly motivated by one of its unique property, namely the ability to generate field-free ensembles of aligned molecules at a predetermined time, independently of the molecular system. To understand the interest of rotational echoes, recall that in "standard" nonadiabatic laser-induced molecular alignment (for a review on molecular alignment and orientation see e.g. Refs. [19–22]), the rotation of the molecules is triggered by a single pump pulse through impulsive nonresonant Raman excitations. This results in an initial alignment of the molecules vanishing shortly after the pulse interaction due to dispersion of the angular velocities associated to excited rotational states of different energy. Thanks to the quantification of the rotational motion and to the initiating pulse of much shorter duration than the rotational period of the molecules, the initial alignment is periodically recovered leading to the so-called alignment revivals [23, 24]. Note that this would continue indefinitely if dissipation [25] and centrifugal distortion [5] were not taken into account. It is easy to understand that the temporal interval between revivals is determined by the moment of inertia of the molecule [20], the smaller the second the larger the first. The fact that the timing of the revivals is tightly bound to the molecule sets a limitation for applications (see later) in which the alignment occurrence must be adjusted independently of the system. On the contrary, rotational echoes can potentially be produced at any time t_E and therefore do not suffer from this drawback. Similarly to spin and photon echoes, rotational echoes are produced by applying to the system two pulses, hereafter referred to as P_1 and P_2, time delayed by τ_{12}. We have shown that it leads to the creation of a main alignment echo centered at time $t_E = 2\tau_{12}$ [1], followed by higher-order echoes, as well as fractional [2], imaginary, and rotated echoes [3]. The adjustability of t_E has been exploited for probing ultrafast collisional relaxation of linear (CO_2) [9] and symmetric-top molecules (C_2H_6) [12], in pure and gas mixtures, for pressure ranges where rotational decoherence could not be measured using standard alignment revivals [25, 26]. By observing the pressure-induced relaxation of the rotational echo during the first few picoseconds following the excitation of N_2O molecules diluted in He, time-domain observation of nonsecular collisional transfers occurring between rotational coherences could be achieved for the first time [10]. This methodology has been recently applied to observe dissipative non-Markovian open quantum system dynamics in CO_2 and HCl molecules [18, 27]. The adjustablity features of the echo were also exploited to significantly improve the alignment of acetone molecule at room temperature, enabling the third-harmonic generation from circularly polarized light otherwise not detectable through alignment revivals of this molecule [15]. Other applications of rotational echoes can be found, as for instance, compensation of the centrifugal distorsion of CH_3I molecule [5], calibration of the degree of laser-induced molecular alignment [7], unidirectional rotation of molecular rotors [14], and high-order harmonic generation [8].

In echo spectroscopy, it is usual to perform measurements for different time occurrences t_E of the echoes. For instance, measuring the decay of the photon echo [28] amplitude versus the delay between the two excitation pulses provides relevant information about decoherence time for homogeneously and inhomogeneously broadened systems [29,30]. This kind of studies is possible because the magnitude of a photon echo does not intrinsically depend on the delay between the two excitations. This is no longer valid for a

Laboratoire Interdisciplinaire CARNOT de Bourgogne, UMR 6303 CNRS-Université de Bourgogne, BP 47870, 21078 Dijon, France;
* Corresponding author: e-mail: olivier.faucher@u-bourgogne.fr

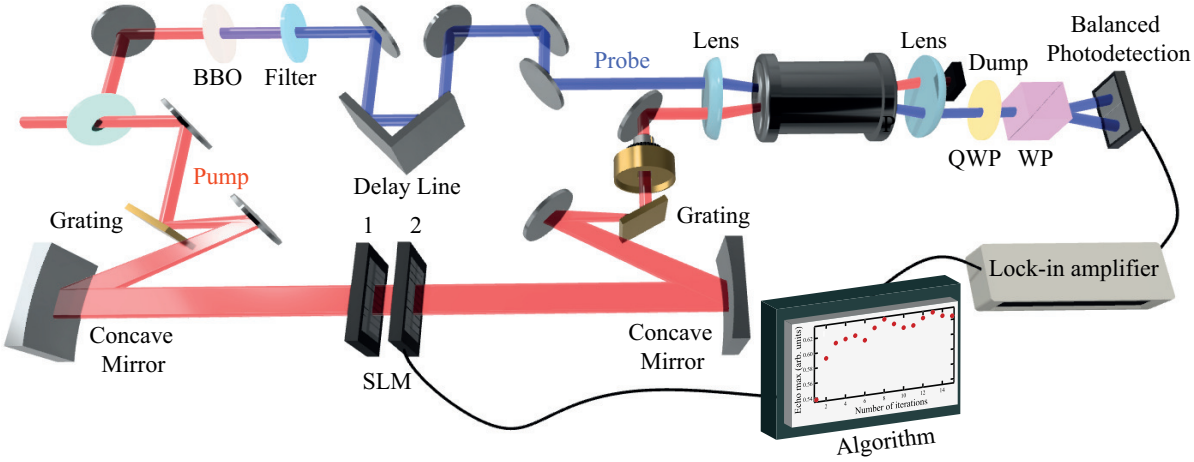

Figure 1 Experimental pump-probe setup used to create a bipulse and optimize the echo amplitude. SLM: one-dimensional dual mask liquid crystal spatial light modulator, P: Glan polarizer, QWP: quarter waveplate, WP: Wollaston prism.

rotational echo where its amplitude is strongly determined by t_E. This effect finds its origin in both the filamentation of the phase space in classical analysis [1] and the multi-level nature of the rotational motion in quantum analysis [6]. However, it has been shown [6] that for each value of the delay τ_{12}, one can find an intensity ($I_{2_{opt}}$) of P_2 that maximizes the echo to the same amplitude regardless of τ_{12}. In practice, the fine adjustment of I_2 is not necessarily easy to implement, especially in quantitative studies involving low signal-to-noise ratio and/or requiring long series of data acquisition. This was for instance the case in Refs. [9, 12] where, in order to improve the accuracy of the measurements, the variation of the delay τ_{12} was limited over a small range so that $I_{2_{opt}}$ could be considered constant over all measurements. However, note that this approach is only applicable to studies where the intrinsic variation of the echo with τ_{12} is small compared to the effect to be measured.

In the present work, we investigate a process for rotational alignment echo spectroscopy which overcomes the constraint due to the intricate dependence of the rotational echo amplitude on I_2 and τ_{12}. It is based on an optimization of the echo amplitude by a shaped laser pulse generated with a spatial light modulator (SLM) feedback-controlled by an evolutionary algorithm. As a proof of principle, we apply the proposed method to measure the pressure-induced decay of the rotational quantum coherences and populations of aligned molecules.

2. Method

2.1. Setup

The experimental setup is represented in Fig. 1. The laser beam produced by a chirped-pulse amplified Ti:Sapphire laser [800 nm central wavelength, 100 fs duration full width at half maximum (FWHM), and 1 kHz repetition rate] is splitted into a pump and probe beam. The former is directed to a pulse shaper which is based on a zero-dispersion 4f line comprising a pair of 1600 lines/mm gratings and 400-mm focal length cylindrical mirrors. A programmable one-dimensional dual mask liquid crystal spatial light modulator (SLM) array is located in the Fourier plane of the 4f line. A polarizer is placed at the output of the 4f line allowing independent control of the spectral phase and amplitude for each of the 320 pixels arrays composing the SLM. The tuning of the temporal delay between the probe pulse, frequency doubled in a type I BBO crystal, and the shaped pump pulse is achieved by a motorized translation stage equipped with a corner cube reflector. The probe beam is then vertically polarized at 45° with respect to the pump beam [using half waveplates and polarizers not represented in Fig. 1] right before both are focused in a gas cell, the overlap between the two foci being optimized by a telescope inserted in the probe beam path. After propagation through the gas cell, the change in polarization of the probe beam is analyzed by a balanced detection [31] providing a signal proportional to the alignment factor $\langle \cos^2\theta \rangle_T - 1/3$ [32], where θ is the angle between the molecule and the polarization direction of the pump pulse and $\langle\rangle_T$ denotes a thermal averaging over the quantum expectation value of the observable $\cos^2\theta$ accounting for the finite temperature T of the medium.

2.2. Pulse shaping

Figure 2(a) provides an example of alignment signal produced by the shaped pulse in low gas pressure of N_2O molecules. The SLM has been programmed so that the pulse shaper produces as outcome two pulses P_1 (intensity I_1) and P_2 (intensity I_2) time shifted by τ_{12}. As shown in Fig. 2(a), each of them is responsible for inertial alignment peaks denoted IAP1 and IAP2, but the combination of both generates the main echo E1 at $2\tau_{12}$, i.e. the echo of interest in the present work, and a second-order echo E2 at $3\tau_{12}$. Note the presence of an elevated base line after the first pulse

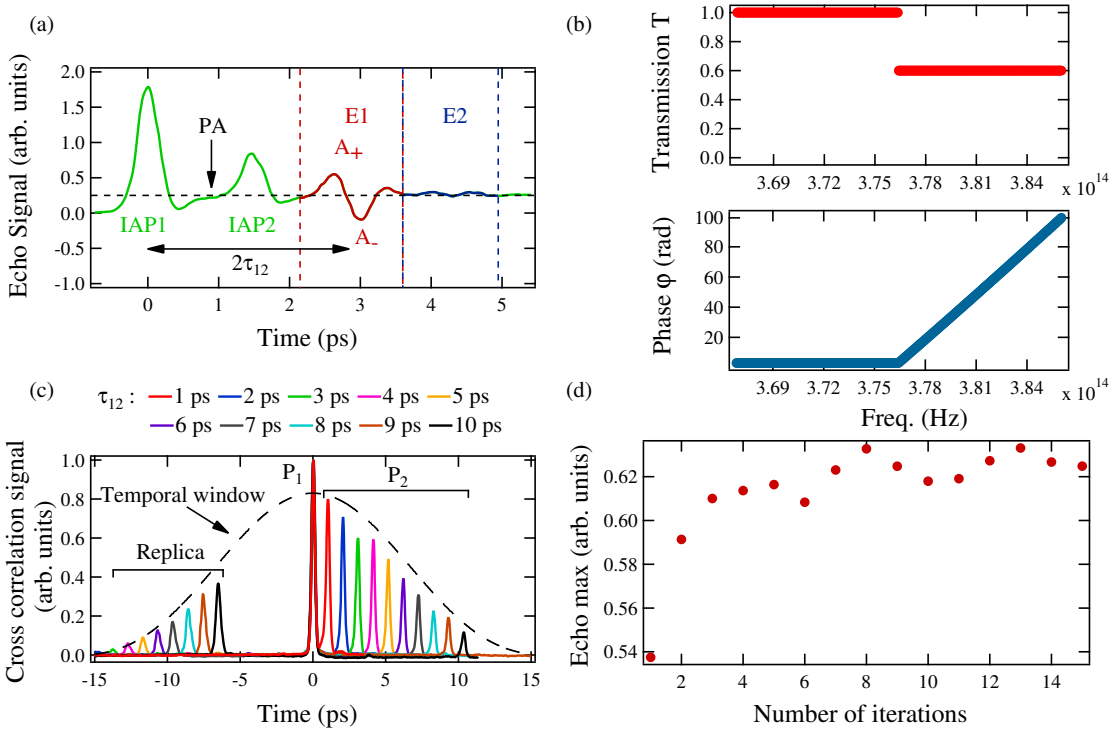

Figure 2 (a) Alignment features produced by pulse shaping in low-pressure N_2O molecule. The inertial alignment peaks IAP1 and IAP2 consecutive to the excitation of the molecule by the pulses P_1 and P_2 (separated by $\tau_{12} = 1.5$ ps), respectively, are depicted in green, whereas the main echo E1 (of maximum and minimum value A_+ and A_-, respectively) and second-order echo E2 are shown in red and blue, respectively. The permanent alignment (PA) is denoted with the dashed black line. (b) Spectral intensity transmission (top) and phase (bottom) generated by the combination of liquid crystal masks depicted in Fig. 1. (c) Cross-correlation signals (solid lines) of the SLM output recorded in Argon. The results are shown for various applied phase modulations corresponding to different generated delays τ_{12} between pulse P_1 ($t = 0$) and P_2 ($t > 0$). The pulse replica ($t < 0$) and the sinc time window envelop (black dashed line) are inherent features related to the pulse shaping technique (see text). (d) Evolution of the fitness function (A_+) versus the number of iterations. The best individuals are depicted as a function of number of iterations.

excitation corresponding to the permanent alignment [20] resulting from the large intensity of P_1 ($I_1 = 20$ TW cm^{-2}). As exemplified by Fig. 2(b), the shaped pulse is synthesized by applying to the right half-part of the SLM input spectrum (i.e. for $\omega > \omega_0$, where ω_0 is the central frequency) an intensity transmission factor $T(\omega)$ and a linear phase shift $\varphi(\omega) = \omega\tau_{12}$. These two parameters determine the delay τ_{12} and the field intensity ratio $R = \frac{I_2}{I_1} \leqslant 1$ between the two pulses, with the pulse P_1 carrying half of the total input energy. The applied phase and transmission modulations are pixelated. Recall that for a given pixel i ($1 < i < 320$) of the liquid crystal SLM array, the transmission and phase are given by $T_i = \cos^2\left(\frac{\phi_{1i} - \phi_{2i}}{2}\right)$ and $\phi_i = \left(\frac{\phi_{1i} + \phi_{2i}}{2}\right)$, where ϕ_{1i} and ϕ_{2i} are the phases induced by each pixel i of masks 1 and 2 depicted in Fig. 1, respectively. The dispersion of the pulse shaper in the Fourier plane has been calibrated in order to estimate the averaged value of the spectral sampling $\Delta\nu$=61.2 GHz/pix. This allows to assess the major pulse distorsions of the SLM related to the pixelated nature of the device. As explained in refs. [33, 34], the shaping of the pulse inherently results in the production of replicas with a time period $\Delta\tau_{rep} = 1/\Delta\nu = 16.3$ ps. In addition, the temporal field consisting of the desired pulse sequence P_1, P_2 and replica is modulated by a sinc time window given by $\mathrm{sinc}(\pi\Delta\nu t)$. The output of the pulse shaper has been characterized by recording in argon the third-order non-collinear cross-correlation Kerr signal between the shaped and probe pulse. The data reported in Fig. 2(c) have been recorded for different phase modulations $\varphi(\omega)$ and same transmission factor $T(\omega) = 1$. They clearly show the pulse P_1 and P_2 generated with a time delay τ_{12}, as well as the replicas produced before P_1 at $t = \tau_{12} - \Delta\tau_{rep}$. The pulse duration of P_1 and P_2 derived from the cross-correlation traces, ~ 185 fs (FWHM), is in good agreement with the calculation (170 fs) obtained from $T(\omega)$ and $\varphi(\omega)$ applied to the pulse shaper and the initial spectral bandwidth of incoming pulse (11 nm FWHM).

2.3. Optimization

The echo optimization is obtained by an evolutionary algorithm programmed to find the best value of T and φ maximizing the peak amplitude A_+ [see Fig. 2(a)] of the echo

measured by the probe pulse at time $t_{pr} \approx t_E = 2\tau_{12}$. The optimization procedure uses a low-dimensional parameterization of the search space. The delay τ_{12} and transmission T applied by the pulse shaper on half part of the spectrum to produce P_1 and P_2 build the genes of the evolutionary algorithm. These two parameters are iteratively optimized by the learning algorithm for maximizing the echo leading to a constant echo amplitude regardless of its creation time. The algorithm starts from a population of 30 individuals composed of randomly chosen genes, bounded within an adequate range. Each individual is experimentally tested by measuring the echo signal by means of a probe pulse timed to a given (fixed) temporal delay t_{pr} with respect to P_1. The fitness A_+ is then used as a feedback signal for the adaptive optimization that uses the concepts of biological evolution. The best six individuals are cloned (elitism) and from these parents, 24 new individuals or "children" are generated. Each child is produced from a random crossing of the genes of two parents. A quarter of them is also subject to the mutation of one of its genes produced by adding a random value within a range that is reduced along the optimization procedure. The new population thus produced is tested and the procedure is repeated until convergence towards an optimum. As shown in Fig. 2(d), convergence is usually achieved after 10 generations. Note that the pump-probe signal presented in Fig 2(a) was recorded after optimization of the echo, i.e. for the optimal intensity $I_{2_{opt}}$ of P_2.

It should be emphasized that the optimization procedure described above is not compromised by the presence of replica and the sinc time window effect described in the previous section. The first reason is that the total energy sent to the pulse shaper can be chosen so that the intensity of pulse P_1 (carrying half of the total energy) is much larger than the one of the replica. The result of this choice is i) to minimize the alignment signal produced by the replica with respect to P_1 and ii) to set the maximum achievable intensity for P_2 (defined by the sinc time window of the SLM and the total energy) above the value required to optimize the echo signal for all delays τ_{12}. The second reason is that the effect of the replica on the echo signal is most noticeable when the echo induced by the replica and P_1 coincides with P_2, which in our case only occurs for $\tau_{12} = 8$ ps. As will be shown in the next section, this does not noticeably affect the optimization of the echo signal.

2.4. Validation of the method

To demonstrate the benefit of our approach, the magnitude of the echo has been recorded for τ_{12} covering a broad temporal domain of 6.5 ps. As for the record of Fig. 2(a), the N_2O pressure in the gas cell was reduced to 0.10 bar to avoid any noticeable collision-induced change in echo amplitude while varying τ_{12}. For each pump-probe delay t_{pr}, the outcome of the shaper was optimized to produce a maximum probe signal, prohibiting the system to overlap the inertial alignment peak of P_2 [shown in Fig. 2(a)] with the probe pulse, which occurs when $t_{pr} \approx \tau_{12}$. The fully automatized record depicted in Fig. 3(a) with red circles

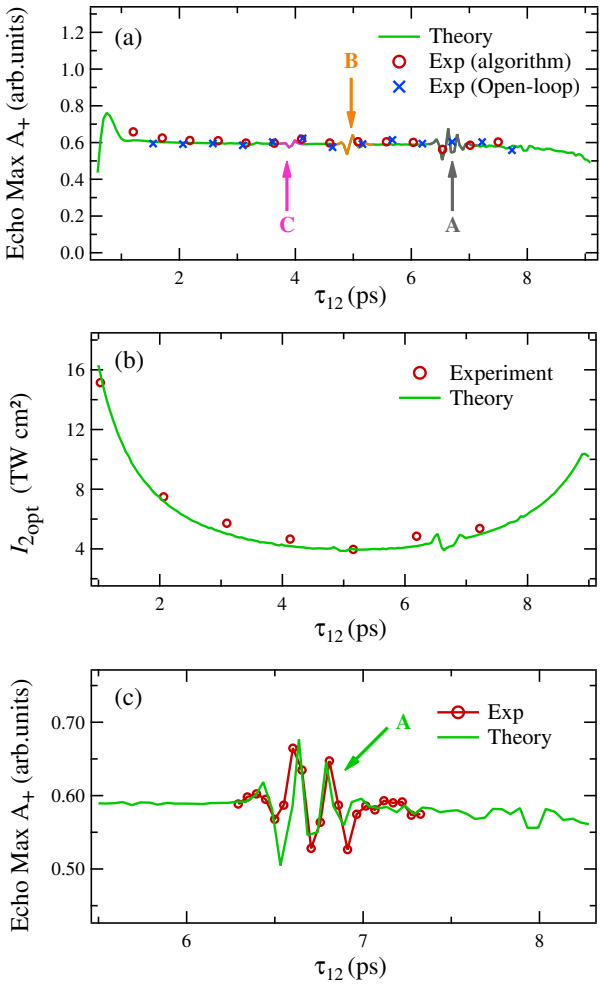

Figure 3 (a) Peak amplitude A_+ of the alignment echo generated in N_2O by pulse shaping versus the delay τ_{12} between the two pulses P_1 and P_2. The experimental data (red circles), obtained by optimizing the phase ϕ_1 and ϕ_2 with the evolutionary algorithm, are compared to numerical simulations (green line) based on FTL pulses. The data obtained by programming the shaper to apply the phases learned from the previous optimization process are depicted with blue crosses. The three features marked with arrows correspond to the overlap of the main echo with the first (A), second (B), and third revival (C) of the imaginary echo (see text), respectively. (b) Optimized intensity $I_{2_{opt}}$ of P_2 (red circles) produced by the pulse shaper for different τ_{12} compared to simulations (green line). (c) Overlap region between the main echo and the first revival of the imaginary echo: simulated (green line) and measured signal (red line and circles).

was obtained for a peak intensity I_1 of P_1 estimated around 20 TW cm^{-2}. Except the three features labeled A, B, and C (discussed at the end of this section), the variation of the echo amplitude is less than $\sim 10\%$ over the whole temporal range corresponding to a tuning of the echo between 2 and 15 ps. This value is to be compared to an amplitude variation of $\sim 300\%$ obtained when the signal is measured for a fixed intensity of P_2 maximizing the echo for $\tau_{12} = 5$ ps. The

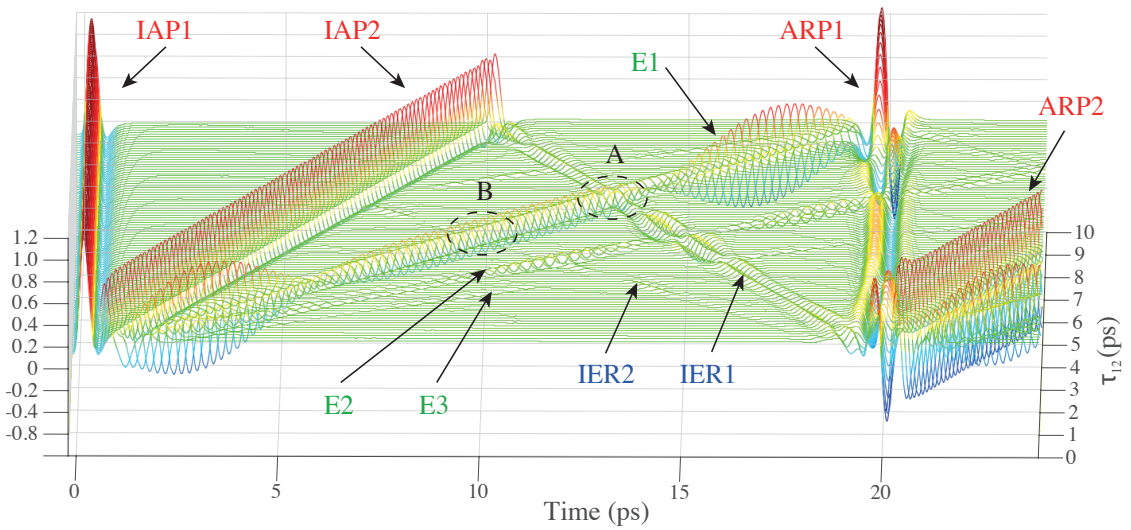

Figure 4 Echo landscape. Molecular alignment features of N_2O produced by two short laser pulses P_1 (20 TW cm^{-2}) and P_2 (13 TW cm^{-2}) calculated for different delays τ_{12} from 0.5 to 9 ps (IAP1 and IAP2, inertial alignment peaks produced by pulse P_1 and P_2, respectively; E1, main echo; E2, 2nd-order echo; E3, 3rd-order echo; IER1, 1st revival of the imaginary echo; IER2, 2nd revival of the imaginary echo; ARP1, 1st alignment revival induced by pulse P_1; ARP2, 1st alignment revival induced by pulse P_2). A and B: temporal overlap zones of the main echo E1 with imaginary echoes IER1 and IER2, respectively.

optimized intensities $I_{2_{opt}}$ versus τ_{12} retrieved from the algorithm and shown in Fig. 3(b) illustrate the strong intricate dependence of the echo with respect to these parameters. These intensities have been estimated taking into account the diffraction effects and pixellation of the SLM addressed in Sec. 2.2. As also shown in Fig. 3(a) with the data depicted with blue crosses, the robustness of the method have been successfully tested in a day-to-day operation by programming the pulse shaper with the outcome previously optimized for each delay τ_{12} without running again the evolutionary algorithm. For further validation of the results, the alignment signal was calculated by solving the Liouville von Neumann equation for different values of τ_{12} and I_2 using Fourier-transform-limited (FTL) pulse P_1 and P_2 of duration equivalent to that produced by the pulse shaper ($\sim$ 185 fs). As shown in Fig. 3(a), the maximal peak amplitude of the echo as a function of τ_{12} is well reproduced by these calculations. The same agreement is found regarding the optimal intensity of P_2 presented in Fig. 3(b). Note that similar calculations based on the amplitude and phase modulation achieved in the experiments lead to the same agreement confirming the weak role played by the replica.

Finally, we would like to address the fast signal modulations observed in Fig. 3(a) (labeled A, B, and C) that are also reproduced by the numerics, as shown for instance in the high resolution measurements of Fig. 3(c). These features result from the overlapping of the main echo with imaginary echoes. The latter phenomenon refers to an echo signal that would be observed at negative time τ_{12} before P_1 if, after applying P_2, one were able to reverse the course of time [3]. In order to better understand the following, calculated alignments features (inertial alignment peaks, alignment revivals, main, higher-order, imaginary echoes, and their respective revivals) are depicted as a function of time in Fig. 4 for fixed P_1 and P_2 intensity. As described in Ref. [3], thanks to the quantification of the rotational energy, the imaginary echo manifests itself at positive instants by its revivals which occur at times $\frac{T_r}{2} - n\tau_{12}$, where $\frac{T_r}{2}$ ($\approx$ 20.22 ps) corresponds to the instant of first revival of N_2O and n refers to n^{th} revival of the imaginary echo. As τ_{12} increases, imaginary echoes (IER1 and IER2) propagate backwards, causing the main echo (E1) to overlap with the first ($n = 1$) and second ($n = 2$) revival of the imaginary echo for $\tau_{12} = \frac{1}{n+2}\frac{T_r}{2} = \frac{T_r}{6} \approx 6.63$ ps (A) and $\frac{T_r}{8} \approx 4.97$ ps (B), respectively. The resulting interferences are responsible for the signal oscillations observed in Fig. 3(a). Note that the third revival ($n = 3$) of the imaginary echo IER3 (C) does not appear in Fig. 4 for the reason that the fixed intensity of P_2 used for calculations does not correspond to the optimal one for the delay leading to the overlap at $\tau_{12} = \frac{T_r}{10} \approx 3.98$ ps.

3. Probing collisional dissipation

Strong-field molecular alignment has proven to be a relevant process to explore the dissipative dynamics of rotational quantum wave packets [10, 25, 35–39]. When dissipation is induced by collisions, it has been shown that the rate of rotational decoherence ($1/T_2$) and population decay ($1/T_1$) can be inferred from the peak-to-dip amplitude of the transient alignment features (revivals [25, 26] and echoes [9]) and from the permanent component of the alignment [25, 26], respectively. The approach presented in the previous section

has been applied to rotational echo spectroscopy for probing short-time collisional dissipation.

The collisional time constant $\tau_E(2\tau_{12})$ of the alignment echo related to the lifetime of rotational coherences was determined for N_2O in Ref. [10] by measuring the peak-to-dip amplitude of the echo generated at time $2\tau_{12}$ as a function of the gas density d for a fixed delay τ_{12}. By repeating this exercise for different τ_{12}, its has been possible to observe a slowdown of the dissipation in the early stage of the system evolution for $1.5 < \tau_{12} < 5$ ps, resulting from nonsecular collisional transfers between rotational coherences [10]. Here, we suggest to follow a different approach. By fixing the gas density d and optimizing the echo for different times $t_E \sim 2\tau_{12}$, we propose to extract from the optimized echo an "average" value of the collisional decay time constant $\overline{\tau}_E$ of the echo. This requires not only to measure the maximum amplitude A_+ of the echo, as in Fig. 3(a), but also its minimum value A_- [see Fig. 2(a)], which are both sensitive to coherence (echo) and population (permanent alignment) decay, in order to extract the peak-to-dip amplitude of the echo $A_E = (A_+ - A_-)$, a quantity that is only related to rotational coherences [25]. To this aim, the algorithm driving the pulse shaper was modified so that for each couple $(\tau_{12_{opt}}, I_{2_{opt}})$ maximizing the echo signal A_+ at time t_{pr}, the delay τ_{12} was tuned by ± 400 fs around $\tau_{12_{opt}}$ by steps of 20 fs in order to localize and measure the minimum A_-. Considering the small range of the delay, this was implemented by applying to the shaper a phase ramp, keeping P_2 intensity ($I_{2_{opt}}$) constant.

3.1. Closed-loop optimization

The experiment was performed by filling the gas cell with 10 bar of room temperature gas mixture of N_2O(5%)-He(95%) corresponding to a N_2O gas density $d = 9.10$ amagat. The results presented in Fig. 5(a) have been obtained by measuring the peak-to-dip amplitude of the optimized echo generated at different times t_{pr} (red circles). The signal exhibits the exponential decay feature expected for collisional relaxation of binary mixtures. To underline the interest of the method, the experimental data were also recorded with a non-optimized P_2 intensity, i.e. with a pulse shaper programmed to produce a bi-pulse with fixed I_2 value regardless of the delay τ_{12} (blue squares). In that case, the variation of the echo results from the intrinsic dependence of its amplitude on τ_{12} (decrease and then increase of the echo with t_{pr}) combined to the pressure effect (decrease of the echo with t_{pr}) which prohibits any direct measurement of the second effect.

3.2. Open-loop optimization

Another benefit of the present optimization method is the possibility to use it in a open-loop configuration. In the context of the present application, the idea was to use the parameters $\tau_{12_{opt}}$ and $I_{2_{opt}}$, learned from the closed-loop optimization conducted in the low-pressure conditions of

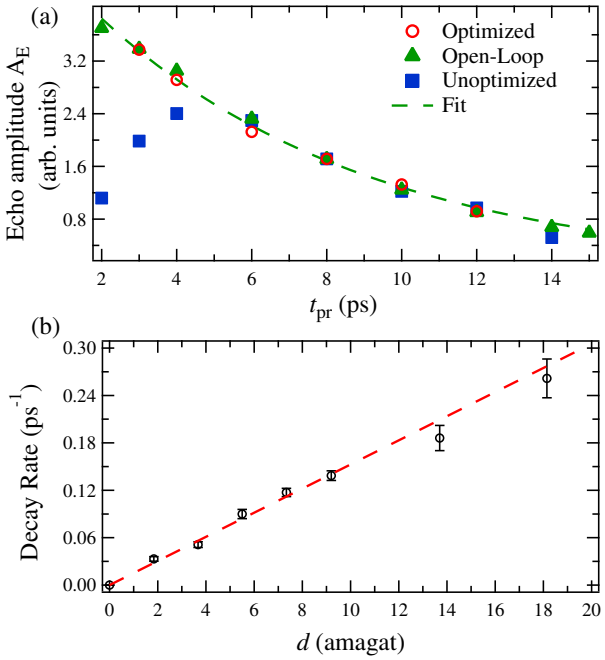

Figure 5 (a) Peak-to-dip echo amplitude recorded in a high-pressure (10 bar) binary gas mixture of N_2O and He at different probe times t_{pr}. Three series of measurements have been performed; i) by optimizing the high-pressure echo signal using the evolutionary algorithm (red circles), ii) by using an unoptimized P_2 intensity set to $I_2 = 4.3$ TW cm^{-2} for all t_{pr} (blue squares), and iii) by programming the pulse shaper to apply the phases learned from the optimization procedure conducted in the low-pressure regime (green triangles). The exponential fit of the data measured with the open-loop procedure is depicted with a green dashed line. (b) Collisional decay rates $\overline{\tau}'_E{}^{-1}$ of the echo measured for various densities d of the gas mixture and linear fit of the data (dashed line).

Fig. 3, to perform measurements in the high-pressure regime in an open-loop configuration, i.e. without implementing new optimizations for each time t_{pr}. Such measurements are presented in Fig. 5(a). They have been implemented with the same gas sample as in the previous measurements. As shown, the data obtained through the open-loop method (green triangles) are similar to those obtained through the closed-loop optimization (red circles), which demonstrates that the optimization method is reliable for operating in open-loop. In addition to saving time, the latter makes it possible to increase the precision of the measurements by offering the possibility to investigate experimental conditions for which the signal-to-noise ratio prohibits an accurate closed-loop optimization of the echo. This was the case in the present study, where for instance the echo recorded in Fig. 5(a) at $t_{pr} < 3$ ps and $t_{pr} > 12$ ps could only be measured using the open-loop mode (or with an unoptimized I_2 intensity). The same has applied for the pressure limit, where the open-loop approach has been used up to 20 bar, while the closed-loop optimization measurements were limited to a maximal pressure of 10 bar. In order to estimate

the density normalized value of τ_E and its uncertainty, the open-loop measurements of Fig. 5(a) have been repeated for different densities d. Figure 5(b) presents the collisional decay rates ${\overline{\tau}'_E}^{-1}$ of each data set least-squared fitted by $\exp\left(-2\tau_{12}/\overline{\tau}'_E\right)$ as well as the linear fit of the all sets leading to the estimated constant $\overline{\tau}_E = \overline{\tau}'_E d = 65 \pm 3$ ps amagat.

Finally, the relaxation of the rotational populations has been obtained by measuring the amplitude $A_P = (A_+ + A_-)/2$ of the permanent alignment versus time. Following the same methodology as in Fig. 5(a), we have derived an estimated collisional time constant value of the permanent component $\tau_P = 321 \pm 35$ ps amagat. The large error bars results from the much larger value of τ_P as compared to τ_E. This difference, already observed in CO_2 molecule [26], is explained by the fact that, due to a gyroscopic effect, the orientation of the rotational angular momentum quantified by M/J, where J is the rotational quantum number and M its projection along the direction of the laser field, is much less sensitive to collisions that the rotational energy quantified by J. In order to improve the accuracy of τ_P, measurements would need to be performed over a much longer temporal range (up to 28 ps) not achievable with the present pulse shaper. Note that in order to improve the accuracy of this constant, the permanent alignment has been conjointly measured by standard (single) pump-probe measurements [26] leading to $\tau_P = 344 \pm 6$ ps amagat.

4. Conclusion

We have shown that the main drawback of molecular alignment echo spectroscopy can be advantageously solved by shaping the phase and amplitude of the aligning field. The proposed method consists in using a spatial light modulator to synthesize a bi-pulse of fixed pulse duration but with delay and amplitude ratio controlled by 2 parameters optimized through a closed-loop evolutionary algorithm. We have demonstrated that such pulse shaping can generate, in a fully automated way, a tunable rotational alignment echo over 15 ps, which is more than enough for most rotational echo spectroscopy applications, with less than $\sim 10\%$ amplitude variation over the entire range. The optimization method has been successfully applied in a closed- and open-loop configuration to measure the collisional decoherence and population decay of aligned N_2O molecules diluted in helium.

Compared to standard optical setup (based on spatially separated beams) for producing bi-pulse of adjustable delay and amplitude ratio, the present optimization method offers significant advantages. First, the two spatial profiles of the pump pulses produced by the pulse shaper perfectly overlap, which is important considering that the echo is a nonlinear process depending on the third power of the pump intensity (for moderate intensity). Second, acquisition times are greatly reduced because the setting of the delay τ_{12} between the two pulses, controlled by the spatial light modulator, requires no moving optics. Third, the maximum of the echo is recorded without the need to scan the delay of the probe pulse since the system automatically adjusts τ_{12} to temporally overlap the echo with the maximum of probe pulse. To quantify the benefit of the last two points, note that measurements like those presented in Fig. 3(a) would take 5 times longer compared to a "traditional" method requiring to store 6 pump-probe traces (one for each delay τ_{12}), with a fine tuning of the intensity of the second pulse between each one. Finally, we have demonstrated that the use of the optimization procedure in a open-loop configuration saves additional time as well as gives access to a wider range of experimental parameters. For all these reasons, we believe that our results will contribute to improve rotational echo spectroscopy and thereby help to develop new applications as for instance 2D spectroscopy [40–42] of systems involving rovibronic resonances or probing dissipation dynamics of slowly rotating molecules like I_2 [43], as well as molecules embedded in nano-droplets [44, 45].

Acknowledgements. The work was supported by the Conseil Régional de Bourgogne Franche-Comté, the EIPHI Graduate School (contract "ANR-17-EURE-0002") and has benefited from the facilities of the SMARTLIGHT platform in Bourgogne Franche-Comté (EQUIPEX+ contract "ANR-21-ESRE-0040").

Key words: Pulse shaping, molecular alignment, rotational alignment echo, ultra-fast laser control.

References

[1] G. Karras, E. Hertz, F. Billard, B. Lavorel, J. M. Hartmann, O. Faucher, E. Gershnabel, Y. Prior, and I. S. Averbukh, Phys. Rev. Lett. **114**(15), 153601 (2015).

[2] G. Karras, E. Hertz, F. Billard, B. Lavorel, G. Siour, J. M. Hartmann, O. Faucher, E. Gershnabel, Y. Prior, and I. S. Averbukh, Phys. Rev. A **94**(3), 033404 (2016).

[3] K. Lin, P. Lu, J. Ma, X. Gong, Q. Song, Q. Ji, W. Zhang, H. Zeng, J. Wu, G. Karras, G. Siour, J. M. Hartmann, O. Faucher, E. Gershnabel, Y. Prior, and I. S. Averbukh, Phys. Rev. X **6**(4), 041056 (2016).

[4] K. Lin, J. Ma, X. Gong, Q. Song, Q. Ji, W. Zhang, H. Li, P. Lu, H. Li, H. Zeng, J. Wu, J. M. Hartmann, O. Faucher, E. Gershnabel, Y. Prior, and I. S. Averbukh, Opt. Express **25**(21), 24917–24926 (2017).

[5] D. Rosenberg, R. Damari, S. Kallush, and S. Fleischer, J. Phys. Chem. Lett. **8**, 5128–5135 (2017).

[6] D. Rosenberg, R. Damari, and S. Fleischer, Phys. Rev. Lett. **121**(23), 234101 (2018).

[7] D. Rosenberg and S. Fleischer, Phys. Rev. Research **2**(2), 023351 (2020).

[8] B. Wang, L. He, Y. He, Y. Zhang, R. Shao, P. Lan, and P. Lu, Opt. Express **27**(21), 30172–30181 (2019).

[9] H. Zhang, B. Lavorel, F. Billard, J. M. Hartmann, E. Hertz, O. Faucher, J. Ma, J. Wu, E. Gershnabel, Y. Prior, and I. S. Averbukh, Phys. Rev. Lett. **122**(19), 193401 (2019).

[10] J. Ma, H. Zhang, B. Lavorel, F. Billard, E. Hertz, J. Wu, C. Boulet, J. M. Hartmann, and O. Faucher, Nature Commun. **10**(1), 5780 (2019).

[11] J. M. Hartmann, J. Ma, T. Delahaye, F. Billard, E. Hertz, J. Wu, B. Lavorel, C. Boulet, and O. Faucher, Phys. Rev. Research **2**(2), 023247 (2020).

[12] J. Ma, H. Zhang, B. Lavorel, F. Billard, J. Wu, C. Boulet, J. M. Hartmann, and O. Faucher, Phys. Rev. A **101**(4), 043417 (2020).
[13] L. Xu, I. Tutunnikov, L. Zhou, K. Lin, J. Qiang, P. Lu, Y. Prior, I. S. Averbukh, and J. Wu, Phys. Rev. A **102**(4), 043116 (2020).
[14] Z. Lian, Z. Hu, H. Qi, D. Fei, S. Luo, Z. Chen, and C. C. Shu, Phys. Rev. A **104**(5), 053105 (2021).
[15] J. Ma, L. H. Coudert, F. Billard, M. Bournazel, B. Lavorel, J. Wu, G. Maroulis, J. M. Hartmann, and O. Faucher, Phys. Rev. Research **3**(2), 023192 (2021).
[16] P. Wang, L. He, Y. He, S. Sun, R. Liu, B. Wang, P. Lan, and P. Lu, Opt. Express **29**(2), 663–673 (2021).
[17] P. Wang, L. He, Y. He, J. Hu, S. Sun, P. Lan, and P. Lu, Opt. Lett. **47**(5), 1033–1036 (2022).
[18] M. Bournazel, J. Ma, F. Billard, E. Hertz, J. Wu, C. Boulet, J. M. Hartmann, and O. Faucher, Phys. Rev.A **107**(2), 023115 (2023).
[19] H. Stapelfeldt and T. Seideman, Rev. Mod. Phys. **75**(2), 543–57 (2003).
[20] S. Fleischer, Y. Khodorkovsky, E. Gershnabel, Y. Prior, and I. S. Averbukh, Isr. J. Chem. **52**(5), 414–437 (2012).
[21] C. P. Koch, M. Lemeshko, and D. Sugny, Rev. Mod. Phys. **91**(3), 035005 (2019).
[22] K. Lin, I. Tutunnikov, J. Ma, J. Qiang, L. Zhou, O. Faucher, Y. Prior, I. Averbukh, and J. Wu, Adv. Photonics **2**(2), 024002 (2020).
[23] F. Rosca-Pruna and M. J. J. Vrakking, Phys. Rev. Lett. **87**(15), 153902/1–4 (2001).
[24] M. D. Poulsen, E. Peronne, H. Stapelfeldt, C. Z. Bisgaard, S. S. Viftrup, E. Hamilton, and T. Seideman, J. Chem. Phys. **121**(2), 783–791 (2004).
[25] S. Ramakrishna and T. Seideman, Phys. Rev. Lett. **95**(11), 113001 (2005).
[26] T. Vieillard, F. Chaussard, F. Billard, D. Sugny, O. Faucher, S. Ivanov, J. M. Hartmann, C. Boulet, and B. Lavorel, Phys. Rev. A **87**(2), 023409 (2013).
[27] M. Bournazel, J. Ma, F. Billard, E. Hertz, J. Wu, C. Boulet, O. Faucher, and J. M. Hartmann, J. Chem. Phys **158**(17) (2023).
[28] N. A. Kurnit, I. D. Abella, and S. R. Hartmann, Phys. Rev. Lett. **13**, 567–568 (1964).
[29] T. Yajima and Y. Taira, J. Phys. Soc. Jpn. **47**(5), 1620–1626 (1979).
[30] M. S. Pshenichnikov, K. Duppen, and D. A. Wiersma, Phys. Rev. Lett. **74**(5), 674–677 (1995).
[31] B. Lavorel, P. Babilotte, G. Karras, F. Billard, E. Hertz, and O. Faucher, Phys. Rev. A **94**(4), 043422 (2016).
[32] V. Renard, M. Renard, S. Guerin, Y. T. Pashayan, B. Lavorel, O. Faucher, and H. R. Jauslin, Phys. Rev. Lett. **90**(15), 153601 (2003).
[33] J. C. Vaughan, T. Feurer, K. W. Stone, and K. A. Nelson, Opt. Express **14**(3), 1314–1328 (2006).
[34] E. Hertz, F. Billard, G. Karras, P. Béjot, B. Lavorel, and O. Faucher, Opt. Express **24**(24), 27702–27714 (2016).
[35] T. Vieillard, F. Chaussard, D. Sugny, B. Lavorel, and O. Faucher, J. Raman Spectrosc. **39**(6), 694–9 (2008).
[36] N. Owschimikow, F. Konigsmann, J. Maurer, P. Giese, A. Ott, B. Schmidt, and N. Schwentner, J. Chem. Phys. **133**(4) (2010).
[37] I. F. Tenney, M. Artamonov, T. Seideman, and P. H. Bucksbaum, Phys. Rev. A **93**(1), 013421 (2016).
[38] R. Damari, D. Rosenberg, and S. Fleischer, Phys. Rev. Lett. **119**, 033002 (2017).
[39] B. A. Stickler, F. T. Ghahramani, and K. Hornberger, Physical Review Letters **121**(24), 243402 (2018).
[40] P. Hamm and M. Zanni, Concepts and Methods of 2D Infrared Spectroscopy (Cambridge University Press, Cambridge, 2011).
[41] J. Lu, Y. Zhang, H. Y. Hwang, B. K. Ofori-Okai, S. Fleischer, and K. A. Nelson, Proc. Natl. Acad. Sci. U.S.A. **113**(42), 11800–11805 (2016).
[42] Y. Park, S. Jin, I. Noda, and Y. M. Jung, J. Mol. Struct. **1168**, 1–21 (2018).
[43] E. F. Thomas, A. A. Søndergaard, B. Shepperson, N. E. Henriksen, and H. Stapelfeldt, Phys. rev. Lett. **120**(16), 163202 (2018).
[44] A. S. Chatterley, L. Christiansen, C. A. Schouder, A. V. Jørgensen, B. Shepperson, I. N. Cherepanov, G. Bighin, R. E. Zillich, M. Lemeshko, and H. Stapelfeldt, Phys. Rev. Lett. **125**(1), 013001 (2020).
[45] J. Qiang, L. Zhou, P. Lu, K. Lin, Y. Ma, S. Pan, C. Lu, W. Jiang, F. Sun, W. Zhang, H. Li, X. Gong, I. S. Averbukh, Y. Prior, C. A. Schouder, H. Stapelfeldt, I. N. Cherepanov, M. Lemeshko, W. Jäger, and J. Wu, Phys. Rev. Lett. **128**(24), 243201 (2022).